I. COLLABORATIVE ANALYSIS OF DIII-D (DoE Grant ER54538)

A. SUMMARY

The collaboration of the Georgia Tech Fusion Research Center in the analysis and interpretation of DIII-D experiments as part of the national DIII-D Team began in 1998 under support from General Atomics and has continued since 1999 under support of DoE OFES (Grant DE-FG02-ER54538). This analysis and interpretation of DIII-D experiments has been closely integrated with the ongoing, internally supported code and theory development in the Georgia Tech Fusion Research Center, and results of both efforts are discussed in this section without distinction. The principal areas of experimental analysis and interpretation have been: 1) the physics of the edge pedestal; 2) density limits caused by thermal instabilities in the plasma edge; 3) plasma rotation; 4) neutral atom fueling and recycling in the plasma edge; and 5) impurity transport in general and the radiating mantle in particular.

B. PHYSICS OF THE EDGE PEDESTAL

1. Background

The 'pedestal' structure of the density and temperature profiles in the edge of H-mode plasmas has been the subject of intensive research for a number of years (see Ref. 1 for review). This interest is motivated in part by the recognition that core transport calculations of the performance of future fusion reactors depend sensitively on the value of the pedestal density and, in particular, the pedestal temperature used as boundary conditions in these calculations[2,3].

Many pedestal investigations have focused on understanding the magnetohydrodynamic (MHD) instabilities that limit the pressure or pressure gradient in the edge pedestal (e.g. Refs. 4-9) or on identifying the experimental relations among MHD instability parameters, device operating parameters, and pedestal parameters (e.g. Refs. 10-13). Correlations of measured pedestal density and temperature values and pedestal profile widths with various MHD and plasma operating parameters have led to theory-based empirical scaling laws (e.g. Ref. 14).

While the MHD instabilities that limit the edge pressure and pressure gradients have been the subject of the majority of the investigations to date, there also have been both i) studies of transport (e.g Refs 15 and 16) and other (e.g Refs.17-19) mechanisms that could cause the formation of the H-mode pedestal and ii) studies of the causes of the observed pedestal structure--widths and gradients of the density and temperature profiles—(e.g. Refs. 20-28). The importance of the ionization of recycling neutrals and of the formation of a negative radial electric field well in determining the edge pedestal structure have been suggested by several of these authors. We note that while the pedestal is modeled

presently in many sophisticated edge and core plasma calculations (e.g. Refs. 29-31) by adjusting transport coefficients in the particle and energy balance equations to obtain agreement with experimental profiles, we are here proposing fundamental studies to determine the causes of the pedestal structure.

2. Work on Edge Pedestal under Grant ER54538

A theoretical model for the density and temperature gradients and widths in the edge pedestal was developed in a series of papers[32-34] from considerations of the MHD stability constraints on the pressure/pressure gradient, of the transport constraints on the temperature and density gradients, and of the observed similarity between the density width and the neutral penetration mean-free-path. This model was tested against DIII-D data[35] and a rough agreement of prediction with experiment was found, but the lack of knowledge of transport coefficients in the edge pedestal and the unavailability of a usable characterization of the MHD stability surface in terms of the edge parameters were identified as impediments to the development of a fully predictive analytical edge pedestal model.

This situation led to an investigation of transport phenomena in the DIII-D edge pedestal[36]. A comparison of various heat conduction theories with data from several DIII-D shots indicated: 1) that neoclassical theory is in somewhat better agreement with experiment than is ITG theory for the ion thermal conductivity, although both agree reasonably well with the thermal conductivity values inferred from the data; 2) that ETG theory ($k_\perp c_s \leq \omega_e$) is in much better agreement with experiment than is electron drift wave theory ($k_\perp c_s \leq \Omega_i$) for the electron thermal conductivity. New theoretical expressions were found for a "diffusive-pinch" particle flux, for the inference of the radial momentum transfer frequency in the edge, and for the density gradient scale length. It was found that neither atomic physics nor convection could account for the inferred momentum transfer rates in the edge, but that gyroviscosity was the right order of magnitude.

The theoretical development of particle transport in the plasma edge directly from the particle and momentum balance equations was extended in a series of papers[37-39] and applied to interpret DIII-D edge pedestal measurements[40]. The resulting calculation model is as follows. The particle and heat balance equations are numerically integrated inward from the separatrix, using separatrix boundary conditions determined from overall energy and particle balances on the plasma within the separatrix, to obtain profiles of the heat (Q) and particle (Γ) fluxes in the plasma edge. The neutral densities needed to evaluate the atomic physics particle sources and heat losses are calculated with a 2D transport model. The heat conduction relations for ions and electrons, $q = (Q-2.5\Gamma T) = nT\chi L_T^{-1}$, are used to determine the radial profile of L_T^{-1} and then the definitions $-(dT/dr)/T = L_T^{-1} = (Q-2.5\Gamma T)/nT\chi$ are integrated radially inward from the separatrix, using experimental separatrix temperature boundary conditions, to calculate

the ion and electron temperature profiles. The heat conductivities inferred from experiment are used to evaluate these expressions.

The momentum balance equations are solved for the requirement $L_p^{-1} = -(dp/dr)/p = (\upsilon_r - \upsilon_{pinch})/D$, where υ_{pinch} denotes a collection of terms involving the radial electric field (E_r), the toroidal and poloidal rotation velocities (υ_φ and υ_θ), the frequency (ν_d*) for the radial transfer of toroidal momentum, and the toroidal components of the beam momentum input and the induced electric field. The radial electric field and the carbon toroidal and poloidal rotation velocities used in the evaluation of υ_{pinch} are taken from experiment. The quantity D denotes another collection of terms arising, as υ_{pinch} does, from the derivation of the relation for L_p^{-1} from momentum balance. The ion density profile is calculated by numerically integrating $-(dn/dr)/n = L_n^{-1} = L_{pi}^{-1} - L_{Ti}^{-1} = (\upsilon_r - \upsilon_{pinch})/D$ inward from the separatrix, using an experimental separatrix density boundary condition.

This coupled nonlinear set of differential equations is iterated to obtain a converged solution for the radial profiles of density, ion and electron temperatures, particle and heat fluxes, and neutral density in the edge plasma. Thus, these profiles are the consequence of 'classical' particle, momentum and energy balance and the heat conduction relation in the presence of recycling neutrals, given the boundary conditions, transport coefficients and radial electric field and the carbon toroidal and poloidal rotation velocities inferred or taken from experiment. Comparison of these profiles with the directly measured experimental density and temperature profiles thus provides a test of whether those profiles can be understood in terms of classical physics—particle, momentum and energy balance plus the heat conduction relation—with the exception that the transport coefficients and the radial electric field and rotation velocities taken from experiment may be produced in part by 'non-classical,' or anomalous, effects.

The principal results of these calculations for one of the five shot/timeslices considered are given in Figs. 1.a-d. Figure 1.a shows the experimental E_r^{exp}, $\upsilon_{\varphi c}^{exp}$, and $\upsilon_{\theta c}^{exp}$ profiles that were used as input, and the profiles of the calculated υ_{pinch} and $\upsilon_r = \Gamma_i/n_i$. It is clear from Fig. 1a that the negative (inward) peaking of υ_{pinch} just inside the separatrix produces (or at least is consistent with) a large negative pressure gradient just inside the separatrix. There is also a peaking of υ_r just inside the separatrix, produced by the ionization of the fueling and recycling neutrals, that enhances the magnitude of the negative pressure gradient just inside the separatrix, but this atomic physics effect is not as large as the effect of the peaking in υ_{pinch}. Similar results were obtained in the other four discharges considered.

The two principal conclusions indicated by these results are: 1) the pedestal structure observed in the edge of H-mode (and some L-mode) plasmas is a natural consequence of the constraints imposed by the conservation of particle, momentum and energy and the heat conduction relations, in the presence of an influx of recycling and fueling neutrals, for the experimentally observed radial electric field and

rotation velocities in the edge; and 2) the major cause of the edge pedestal structure is the large peaking in υ_{pinch} just inside the separatrix. The pinch velocity is caused primarily by the rotation velocity and the radial electric field; thus the remaining questions in understanding the pedestal structure would seem to be related to the causes of the observed rotation velocities and radial electric field in the edge plasma.

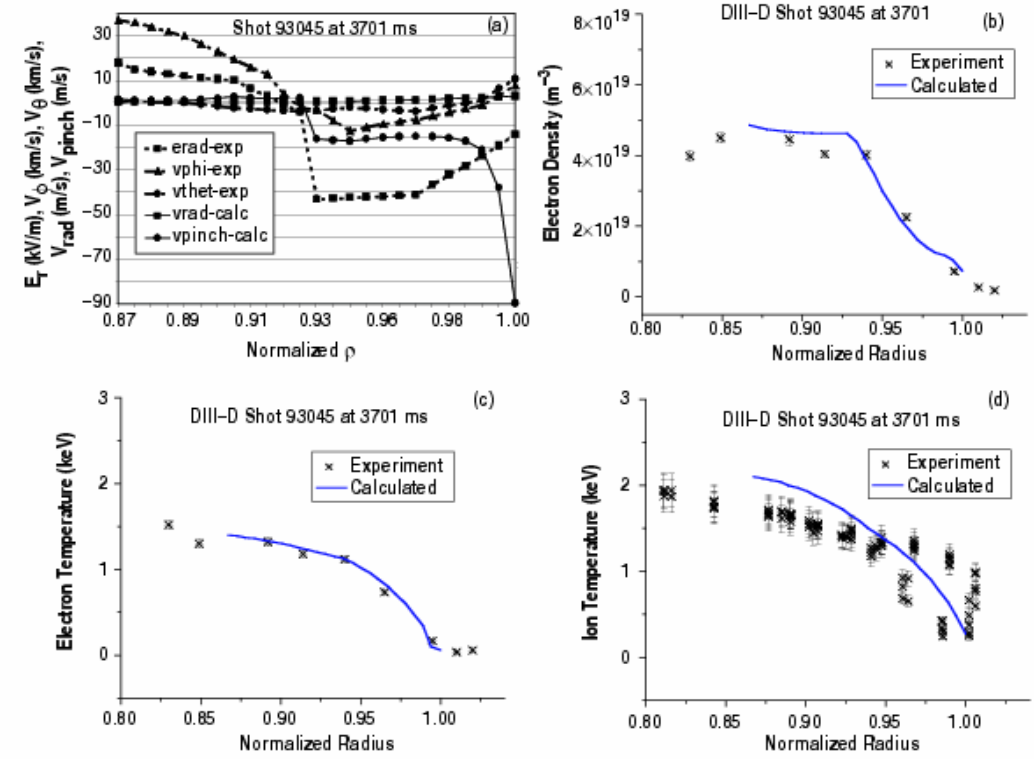

Figure 1: Edge pedestal profiles for DIII-D H-mode discharge 93045 calculated using experimental E_r, V_φ, V_θ and experimental separatrix boundary conditions : a) quantities involved in calculating the pressure gradient; b) calculated and measured n_e profiles; c) calculated and measured T_e profiles; d) calculated and measured T_i profiles.

The calculation for one discharge was repeated with the radial electric field and poloidal rotation velocities also being calculated from momentum balance. The calculated profiles were in somewhat better agreement with the measured profiles than when the experimental values of the radial electric field and poloidal rotation velocities were used in the calculation. Thus, it may well be that both the density and temperature profile pedestal structure and the associated radial electric field and rotation velocity profiles in the plasma edge are natural consequences of classical physics--particle, momentum and energy conservation and the heat conduction relations—but this remains to be established by a more extensive investigation.

3. References for Edge Pedestal

1. A.E. Hubbard, Plasma Phys. Controlled Fusion, 42, A283 (2000).
2. M. Kotschenreuther, W. Dorland, Q. P. Liu, *et al.*, Proc. 16th Conf. Plasma Phys. Control Fusion Research (Montreal, 1996) (IAEA, Vienna, 1997), Vol. 2, p.371.
3. J. E. Kinsey, R. E. Waltz and D. P. Schissel, Proc. 24th EPS, Berchtesgarten, 1997, Vol. III, p. 1081.
4. R. L. Miller, Y. R. Lin-Liu, T. H. Osborne and T. S. Taylor, Plasma Phys. Control. Fusion, 40, 753 (1998).
5. J. W. Connor, R. J. Hastie, H. R. Wilson and R. L. Miller, Phys. Plasmas, 5, 2687 (1998).
6. H. R. Wilson and R. L. Miller, Phys. Plasmas, 6, 873 (1999).
7. B. N. Rogers and J. F. Drake, Phys. Plasmas, 6, 2797 (1999).
8. P. B. Snyder, H. R. Wilson, J. R. Ferron, *et al.*, "Modification of High-Mode Pedestal Instabilities Based on Coupled Peeling-Ballooning Modes", Phys. Plasmas, 9, 2037 (2002).
9. P. B. Snyder, H. R. Wilson, J. R. Ferron, *et al.*, Nucl. Fusion, 44, 320 (2004).
10. R. J. Groebner and T. H. Osborne, Phys. Plasmas, 5,1800 (1998).
11. T. H. Osborne, J. R. Ferron, R. J. Groebner, *et al.*, Plasma Phys. Control. Fusion, 42, A175 (2000).
12. W. Suttrop, O. Gruber, B. Kurzan, *et al.*, Plasma Phys. Control. Fusion, 42, A97 (2000).
13. J. R. Ferron, M. S. Chu, G. L. Jackson, *et al*., Phys. Plasmas, 7, 1976 (2000).
14. T. Onjun, G. Bateman, A. H. Kritz, *et al.*, Phys. Plasmas, 9, 5018 (2002).
15. F. L. Hinton and G. M. Staebler, Phys. Fluids B, 5, 1281 (1993).
16. W. M. Stacey, Phys. Plasmas, 9, 3082 (2002).
17. K. C. Shaing and E. C. Crume, Phys. Rev. Lett., 63, 2369 (1989); K. C. Shaing, E. C. Crume and W. A. Houlberg, Phys. Fluids B, 2, 1492 (1990).
18. A. B. Hassam, T. M. Antonsen, J. F. Drake and C. S. Lui, Phys. Rev. Lett., 66, 309 (1991).
19. P. N. Gudzar, R. G. Kleva, R. J. Groebner and P. Gohil, Phys. Plasmas, 11, 1109 (2004).
20. W. M. Stacey, Phys. Plasmas, 8, 4073 (2001).
21. R. J. Groebner, M. A. Mahdavi, A. W. Leonard, et al., Phys. Plasmas, 9, 2134 (2002).
22. W. M. Stacey and R. J. Groebner, Phys. Plasmas, 10, 2412 (2003).
23. R. J. Groebner, M. A. Mahdavi, A. W. Leonard, et al., Nucl. Fusion, 44, 204 (2004).
24. W. M. Stacey, Phys. Plasmas, 11, 1511 (2004).
25. R. J. Groebner, M. A. Mahdavi, A. W. Leonard, *et al.*, Nucl. Fusion, 44, 204 (2004).
26. C. S. Chang, S. Ku and H. Weitzner, Phys. Plasmas, 11, 2649 (2004).
27. W. M. Stacey, "Structure of the edge density pedestal in tokamaks", Phys. Plasmas, to be published (2004).
28. W. M. Stacey, "Edge pedestal structure", Phys. Plasmas, submitted (2004).
29. G. D. Porter, R. Isler, J. Boedo and T. D. Rognlien, Phys. Plasmas, 7, 3663 (2000).
30. A. Kallenbach, Y. Andrew, M. Beurskens, *et al.*, Plasma Phys. Control. Fusion, 46, 431 (2004).
31. G. W. Pacher, H. D. Pacher, G. Janeschitz, *et al.*, Plasma Phys. Control. Fusion, 46, A257 (2004).
32. W. M. Stacey, "An edge pedestal model based on transport and atomic physics", Phys. Plasmas, 8, 4073 (2001).
33. W. M. Stacey, "An edge pedestal model", Contrib. Plasma Phys., 42, 283 (2002).
34. W. M. Stacey, "An edge pedestal investigation for high-confinement tokamak plasmas", Phys. Plasmas, 9, 1332 (2002).
35. W. M. Stacey and R. J. Groebner, "A framework for the development and testing of an edge pedestal model: formulation and initial comparison with DIII-D data", Phys. Plasmas, 10, 2412 (2003).
36. W. M. Stacey, "Investigation of transport in the DIII-D edge pedestal", Phys. Plasmas, 11, 1511 (2004).

37. W. M. Stacey, "Particle transport and density gradient scale lengths in the edge pedestal", Contrib. Plasma Phys., 44, 100 (2004).
38. W. M. Stacey, "Structure of the edge density pedestal in tokamaks", Phys. Plasmas, to be published (2004).
39. W. M. Stacey, "Edge pedestal structure", Phys. Plasmas, to be published (2004).
40. W. M. Stacey and R. J. Groebner, "Application of a particle, momentum and energy balance model to calculate the structure of the edge pedestal in DIII-D", Phys. Plasmas, to be submitted (in internal review) (2004).

C. THERMAL INSTABILITIES IN THE PLASMA EDGE

1. Background

A number of phenomena are routinely observed in tokamak plasmas in which an equilibrium or slowly evolving set of density and temperature distributions suddenly undergoes an abrupt transition to a quite different set of density and temperature distributions. Perhaps the most dramatic of these abrupt transitions is the collapse of the radial temperature profile, accompanied by the contraction of the current channel, leading to large-scale MHD activity and disruption. The collapse of the radial temperature distribution leading to these 'density limit' disruptions has been identified as a thermal instability in the radial energy and particle balances driven by low-Z radiation cooling in the plasma edge[1-3].

Another familiar example of a thermal instability is MARFE formation, in which a poloidally uniform temperature and density distribution in the plasma edge just inside the LCFS suddenly evolves into a highly non-uniform edge plasma distribution characterized by a poloidally localized and highly radiating region of high density and low temperature, usually located on the low-field inboard side in limited discharges and near the x-point in diverted discharges. This abrupt transition has been identified as a thermal instability in the density, momentum and energy balance along the field lines just inside the LCFS driven by either low-Z impurity radiation cooling[4] or charge-exchange and ionization cooling due to recycling neutrals[5].

Disruptions, MARFEs and other phenomena which can be understood as manifestations of thermal instabilities in the plasma edge or divertor appear to play a role in determining the maximum density that can be achieved in tokamaks. For example, in DIII-D diverted discharges, the following sequence is observed with continuous gas fueling[6-10]: 1) the plasma partially detaches from the outboard limiter and a dense, cool and highly radiating region forms just in front of the divertor plate; 2) at a somewhat later time, this dense, radiating region moves abruptly upstream in the divertor plasma to the vicinity of the x-point, forming a so-called 'divertor MARFE'; 3) with continued gas fueling, the confinement deteriorates and 4) a core MARFE is formed inside the separatrix in the vicinity of the x-point; 5) followed immediately by a H-L transition. On the other hand, ohmic heated and high-Z_{eff} auxiliary heated limited discharges in TEXTOR with continuous fueling tended to detach symmetrically when the radiated power reached 100% of the input power and then undergo a radiative collapse of the

temperature profile and disrupt[11], while auxiliary heated discharges and the low-Z_{eff} ohmic heated discharges tended to form MARFEs followed by a radiative collapse and disruption[12,13].

Thus, it seems clear that an understanding of thermal instability phenomena in the edge and divertor plasmas can make an important contribution to understanding a number of phenomena related to the density limit in tokamaks.

2. Work on Thermal Instabilities in Tokamak Edge Plasmas

For a number of years we have undertaken a systematic development of predictive onset conditions for various thermal instabilities in the plasma edge and the application of these predictions to understand various density-limiting phenomena in DIII-D. The predictive models for thermal instability onset have been incorporated into a code[14,15] for modeling the edge plasma conditions (core particle and power balances, 2-point divertor plasma model, 2D fueling and recycling neutral atom transport), This code uses whatever data that are available from experiment and calculates the other parameters (e.g. atomic physics reaction rates in edge and divertor plasmas) that are needed to evaluate the thermal instability onset predictions.

The development of a predictive onset condition for a particular thermal instability was developed by performing a linear stability analysis of the governing particle, energy and (in some cases) momentum balance equations for a specific type of perturbation about a given equilibrium solution to the governing equations. This led to a dispersion relation, from which a solution for the linear growth rate could be found, either analytically or numerically. The condition for the vanishing of the linear growth rate defined the threshold condition for the onset of the respective thermal instability. This threshold condition was then, when possible, solved for a threshold value of some parameter (e.g. the density) above which the thermal instability grew.

Collapse of radial temperature profile leading to disruption

The onset conditions for collapse of the radial temperature distribution leading to disruption were determined first from a simplified treatment of the radial distribution[16] and then with a distributed model[17] by evaluating the linear stability of the radial particle and energy balance equations in the edge and core to perturbations $\delta n \sim \delta T \sim J_0(5.5r/a)$ which represent a temperature decrease in the outer region $2.4 < r/a < 5.5$ and an increase in the inner region. The threshold condition can be expressed as a threshold line-averaged density above which a density limit disruption would be predicted. The threshold density increases with the thermal conductivity in the core and decreases with impurity radiation term, $f_z(-\partial L_z/\partial T)$. This radiative collapse onset calculation is routinely made in analyzing DIII-D shots, and the threshold density prediction is well above the measured density in those shots that do not disrupt. In the

half-dozen shots examined that did disrupt, the measured line-average density exceeded the threshold density late in the discharge.

MARFE Onset

The onset condition for MARFE formation was derived by considering the linear stability of the 3D particle, momentum and energy balance equations in a thin band just inside the LCFS to toroidally symmetric perturbations primarily along the field lines, but with small radial extent as well[18-24]. The onset condition could be expressed as a threshold edge plasma density, the value of which increased with the heat flux flowing radially across the edge, decreased with the concentrations of low-Z impurity and neutral atoms in the edge, and had a rather complicated temperature dependence reflecting the temperature dependence of the impurity radiation emissivity and the atomic physics cooling rates as well as an explicit 1/T dependence.

This MARFE onset condition, n_{marfe}, was evaluated for a number of times during several "density limit" discharges with continuous gas fueling in DIII-D[25-29]. It was found that the time at which the increasing value of the measured edge density became as large as the calculated MARFE threshold density was very close to the time at which the x-point MARFE formation was observed experimentally, as shown in Table 1. Similar discharges in which MARFEs were neither observed nor predicted are indicated by "none". (The divertor MARFE onset shown in this table will be discussed later.)

It is noted that the MARFE onset prediction has no explicit q_{95}-dependence. Yet it is clear from Table 1 that the line average density at which a MARFE occurred, normalized to the Greenwald density $n_{GW} = I/\pi a^2$, depended inversely on q_{95} and that this dependence was predicted. The likely explanation is that some of the measured edge parameters that were used to evaluate the onset prediction depend on the parallel path length of the scrape-off layer and divertor channel along the field lines and this path length can be characterized by $L_{\|} \sim q_{95;}$ e.g. the longer $L_{\|}$ the more radiative and recycling neutral cooling and the lower the edge temperature, other things being the same.

Divertor MARFE Onset

A prediction for the onset of divertor MARFEs was developed[30] by examining the stability of the one-dimensional particle, momentum and energy balance equations along field lines in the divertor plasma to perturbations along the field lines with scale length comparable to the distance from the divertor plate to the x-point. The resulting dispersion relation is sufficiently complicated that numerical evaluation is required to determine the growth rate. Examination of the dispersion relation indicates that impurity radiation, atomic physics cooling and the particle flux from the core into the SOL are destabilizing, while the heat flux from the core into the SOL and volumetric recombination are stabilizing.

Table 1: **MARFE onset prediction for gas-fueled DIII-D shots**
(R = 1.70-1.76 m, a = 0.6 m, κ = 1.70-1.75)

Shot #	P_{NB} (MW)	q_{95}	n/n_{GW} @ t_{marfe}	MARFE t_{marfe}^{exp} (s)	MARFE t_{marfe}^{calc} (s)	DIVMARFE $t_{divmarfe}^{exp}$ (s)	DIVMARFE $\omega_{div}>0$ (s)
92980	9.5	6.0	0.73	3.53	3.5-3.6		
92796	5.0	6.0	0.67	3.05-3.10	3.0-3.2	2.70-2.90	2.70-2.75
92983	2.5	6.0	0.58	2.90-3.00	2.6-2.8		
92972	5.0	3.0	0.95	3.05-3.15	3.0-3.2		
97979	6.5	3.8	0.81	None	None		
100308	4.5	3.1	0.96	None	None		
98893	2.0	3.5	1.40	None	None		
101560	4.6	4.2	0.79	4.80-4.90	4.8-4.9	4.65-4.80	4.50-4.80
101565	4.7	4.0	0.80	4.80-4.90	4.8	4.60-4.85	4.60-4.80
101626	3.4	4.2	0.81	None	None	None	None
101627	4.8	4.2	0.75	None	None	None	None
102447	4.5	4.0	0.79	4.90-4.98	4.8-4.9	4.70-4.90	4.80-4.90
102858	4.5	4.3	0.77	3.90-4.53	4.2-4.4	4.10	4.00-4.20
102859	4.7	4.1	0.74	4.10-4.25	4.0-4.2	4.10-4.30	4.0
102461	2.5	2.9	0.95	None	None		
102456	2.5	3.9	0.79	3.30-3.33	3.30-3.33		

The conditions in the divertor were evaluated for several DIII-D shots and the time intervals within which the linear growth rate became positive were determined for several DIII-D discharges and found to be in agreement with the times for which divertor MARFEs were observed experimentally, as indicated in Table 1.

Transport Enhancement

The possibility that transport enhancement associated with short radial wavelength thermal instabilities in the edge could be responsible for the L-H transition or for the H-mode confinement degradation observed experimentally was investigated[31-33] by performing a linear stability analysis of the particle, momentum and energy balance equations in the plasma edge to 2D (r, $\perp$) perturbations about an equilibrium solution.

A dispersion relation for the growth rates of thermal instability modes associated with ion and electron temperature instabilities of the form

$$\omega = -\frac{2}{3}\left(\chi\left(\nu L_T^{-2} + k_r^2\right) + \frac{5}{2}\nu\frac{\Gamma_\perp}{n}L_T^{-1} - \alpha \right), \qquad (1)$$

was found, where the radiation and atomic physics terms differed for the ions

$$\alpha_i = \frac{5}{2}(\nu - 1)\nu_{ion} + \frac{3}{2}\nu_{at}^c\left(\nu - \left[1 + \frac{T_i}{\nu_{at}^c}\frac{\partial \nu_{at}^c}{\partial T_i}\right]\right) - \frac{1}{n}\left(\nu\frac{H_i}{T_i} - \frac{\partial H_i}{\partial T_i}\right) \qquad (2)$$

and the electrons

$$\alpha_e = n_z\left(\frac{\nu L_z}{T_e} - \frac{\partial L_z}{\partial T_e}\right) + \nu_{ion}\left\{\frac{5}{2}(\nu - 1) + \nu\frac{E_{ion}}{T_e} - \left(\frac{3}{2} + \frac{E_{ion}}{T_e}\right)\frac{T_e}{\nu_{ion}}\frac{\partial \nu_{ion}}{\partial T} - \frac{1}{n}\left(\nu\frac{H_e}{T_e} - \frac{\partial H_e}{\partial T_e}\right)\right\}. \quad (3)$$

Here $\chi_r \sim T^\nu$ was used, $L_T^{-1} = -(dT/dr)/T$, and H is any external heating in the pedestal.

Assuming that the transport enhancement associated with these thermal instabilities can be represented by Kadomtsev's connection length expression $\Delta\chi \approx \omega k_r^{-2}$ and that the background transport in the absence of thermal instabilities is χ^0, Eq. (1) was solved for the threshold value of L_T for which $\omega = 0$. Using the heat conduction relation, this threshold L_T can be converted to a threshold for the non-radiative power crossing the separatrix

$$P_{thresh} = \frac{5}{4}\Gamma_r T A_{sep}\left[\sqrt{1 + \frac{\left(\chi^0\left(\alpha - \chi^0 k_r^2\right)/\nu\right)}{\frac{5}{4}\frac{\Gamma_r}{n}}} + 1\right] \quad (4)$$

where A_{sep} is the area of the separatrix.

The sum of $P_{threshi}$ for the ions and $P_{threshe}$ for the electrons was compared with the measured power crossing the separatrix, P_{sep}^{exp}, as shown in Table 2, for both L-H and H-L transitions with a wide range of edge conditions[34,35]. A value $k_r^{-1} = 1$ cm was used in the comparison because $\Delta\chi \approx \omega k_r^{-2}$ can exceed the representative H-mode thermal conductivity $\chi^0 \approx 0.1$ m^2/s for typical growth rates of $\omega > 10^3$/s. Clearly, there is agreement between the predicted power threshold of Eq. (4) and the measured power crossing the separatrix at the L-H and H-L transitions in these discharges, suggesting that the stabilization of $k_r^{-1} \approx 1$ cm thermal instabilities in the edge pedestal could be involved in triggering the L-H transition, and conversely that destabilization of $k_r^{-1} \approx 1$ cm thermal instabilities could be involved in triggering the H-L transition.

Table 2 **Some DIII-D shots just prior to the L-H or H-L transition** (R=1.71-1.79m, a=0.6m, κ=1.73-1.89, LSN divertor, $\chi^0 = 0.1\ m^2/s$, $k_r^{-1} = 1$ cm)

Shot #	*Time (ms)*	*I (MA)*	*B (T)*	P_{NB} *(MW)*	n_{eped} *(e19/m^3)*	T_{eped} *(eV)*	P_{sep}^{exp} *(MW)*	P_{thr} *(MW)*
L-H								
102456	1725	1.4	2.0	2.6	3.22	95	1.55-1.86	1.54
97979	1900	1.4	2.0	2.0	2.59	125	1.72-2.04	2.18
92079	2275	1.0	2.1	6.8	1.28	220	3.99-4.06	4.00
84027	2575	1.3	2.1	1.1	2.94	144	1.28-1.36	1.13
H-mode								
97979[a]	3250	1.4	2.0	6.5	6.35	525	4.64-4.96	2.59
H-L								
92976	3210	1.0	2.1	5.0	4.95	275	3.96-4.33	4.21
101565	4950	1.4	2.0	4.7	6.75	170	4.21-4.85	4.60
102456	3500	1.4	2.0	2.4	6.25	150	2.48-2.82	2.36
102461	3300	1.4	1.5	2.4	7.80	170	2.11-2.17	2.18

[a] well into H-mode phase, not at the L-H of H-L transition—control case

It is widely observed in DIII-D H-mode discharges in which it is attempted to build up the density by continuous gas fueling that the energy confinement time and the steepness of edge pedestal density and temperature gradients all decrease with continued fueling. The destabilization and growth of short radial wavelength instabilities of the type discussed above, but with shorter radial wavelengths $k_r^{-1} < \sqrt{\chi^0/\omega}$ that would cause a much less dramatic transport enhancement, could be responsible for the observed deterioration of χ and L_T^{-1} in the edge pedestal. The above equations were evaluated[26] for the ion temperature instability growth rate at several times in some continuously gas fueled DIII-D discharges in which the energy confinement times were observed to deteriorate with time. The calculations were made for $k_r^2 << \nu L_T^{-2}$ so that k_r^2 could be neglected in Eq. (1). The increase with time of the calculated growth rate and the decrease with time of the measured $H_{89P} = \tau_{exp}/\tau_{iter89p}$ (based on the ITER-89P scaling law) appeared to be correlated.

A review[36] of thermal instabilities in tokamaks was prepared.

3. References for Thermal Instabilities

1. A. Gibson, Nucl. Fusion, 16, 546 (1976).
2. N.Ohyabu, Nucl. Fusion, 19, 1491 (1979
3. C. E. T. F. Ashby and M. H. Hughes, Nucl. Fusion, 21, 911 (1981).
4. J. F. Drake, Phys. Fluids, 30, 2429 (1987).
5. M. Z. Tokar, Phys. Scr. 31, 411 (1985).
6. T. W. Petrie, A. G. Kellman and M. A. Mahdavi, Nucl. Fusion, 33, 929 (1993).
7. T. W. Petrie, D. N. Hill, S. L. Allen, et al., Nucl. Fusion, 37, 321 (1997).
8. T. W. Petrie, S. L. Allen, T. N. Carlstrom, et al., J. Nucl. Mater., 241-243, 639 (1997).
9. R. Maingi, M. A. Mahdavi, T. C. Jernigan, et al., Phys. Plasmas, 4, 1752 (1997).
10. W. M. Stacey and T. W. Petrie, Phys. Plasmas, 7, 4931 (2000).
11. G. Waidmann and G. Kuang, Nucl. Fusion, 32, 645 (1992).

12. J. Rapp, P. C. De Vries, F. C. Schuller, et al., Nucl. Fusion, 39, 765 (1999).
13. U. Samm, P. Bogen, G. Esser, et al., J. Nucl. Mater., 220-222, 25 (1995).
14. W. M. Stacey, "A coupled plasma-neutrals model for divertor simulations", Phys. Plasmas, 5, 1015 (1998).
15. W. M. Stacey, "A calculation model for density limits in auxiliary heated, gas fueled tokamaks and applications to DIII-D model problems", Phys. Plasmas, 8, 3673 (2001).
16. W. M. Stacey, "Radial thermal stability of the radiative mantle", Phys. Plasmas, 3, 1012 (1996).
17. W. M. Stacey, "Density limits in tokamaks", Phys. Plasmas, 4, 1069 (1997).
18. W. M. Stacey, "Explanation for MARFE formation and subsequent evolution into a detached symmetric plasma edge", Phys. Plasmas, 3, 2673 (1996).
19. W. M. Stacey, "Multifaceted asymmetric radiation from the edge; impurity density limits in tokamaks with poloidal asymmetry and rotation", Phys. Plasmas, 3, 3032 (1996).
20. W. M. Stacey, "Multifaceted asymmetric radiation from the edge suppression by external edge heating", Phys. Plasmas, 4, 134 (1997).
21. W. M. Stacey, "Validity of the impurity entrainment assumption the thermal stability analysis of multifaceted asymmetric radiation for the edge in tokamak plasmas", Phys. Plasmas, 4, 242 (1997).
22. W. M. Stacey, "Thermal stability of the tokamak plasma edge", Plasma Phys. Control. Fusion, 39, 1245 (1997).
23. W. M. Stacey, "Density limits for multifaceted asymmetric radiation from the edge", Fusion Technol., 36, 38 (1999).
24. W. M. Stacey, "Effect of convection on multifaceted asymmetric radiation from edge density limits", Phys. Plasmas, 7, 3464 (2000).
25. W. M. Stacey, M. A. Mahdavi, R. Maingi and T. W. Petrie, "Multi-faceted asymmetric radiation from the edge formation in DIII-D high-confinement mode discharges with continuous gas puffing", Phys. Plasmas, 6, 3941 (1999).
26. W. M. Stacey and T. W. Petrie, "The role of thermal instabilities in limiting the density in DIII-D", Phys. Plasmas, 7, 4931 (2000).
27. W. M. Stacey, "A calculation model for density limits in auxiliary heated, gas fueled tokamaks and application to DIII-D model problems", Phys. Plasmas, 8, 3673 (2001).
28. W. M Stacey, T. W. Petrie and A. W. Leonard, "Thermal instability explanation of similar density limits in gas fueled DIII-D H-mode shots with different operating conditions", Phys. Plasmas, 9, 888 (2002).
29. W. M. Stacey, T. W. Petrie and T. H. Osborne, "Thermal instability analysis of different types of density limits in DIII-D gas-fueled, high-mode discharges", Phys. Plasmas, 9, 4174 (2002).
30. W. M. Stacey, "Detachment and divertor temperature and density redistribution", Phys. Plasmas, 8, 525 (2001).
31. W. M. Stacey, "Thermal Instabilities in the edge transport barrier", Phys. Plasmas, 6, 2452 (1999).
32. W. M. Stacey, "Edge pedestal deterioration in tokamak high-mode discharges", Phys. Plasmas, 8, 5199 (2001).
33. W. M. Stacey, "Spontaneous edge transport barrier formation due to suppression of edge thermal instabilities as a low-high trigger mechanisms in tokamaks", Phys. Plasmas, 9, 3082 (2002).
34. W. M. Stacey and T. W. Petrie, "Testing of an edge thermal instability model for the high-to-low mode power threshold", Phys. Plasmas, 10, 3949 (2003).
35. W. M. Stacey, "Testing of an edge thermal instability stabilization model for the low-to-high mode power threshold", Phys. Plasmas, 11, 686 (2004).
36. W. M. Stacey, "A review of thermal instabilities in tokamak plasmas", Nucl. Fusion, submitted (2004).

D. PLASMA ROTATION

1. Background

Plasma rotation in tokamaks is of interest because of its ability to stabilize the resistive wall mode by effectively making the wall more conductive[1], because of its potential to quench turbulent transport via flow shear[2], because of the effects of inertial forces on equilibria[3] and transport[4], and because of the insight that it can provide about transport mechanisms. There is a great deal of plasma rotation data for DIII-D, correlation analysis[5] of which suggests that the same physics governs momentum and ion energy

transport. Momentum transport is widely considered to be anomalous, because the familiar perpendicular neoclassical momentum transport[6-8] is too small by two orders of magnitude to agree with experimental momentum damping rates, but the less familiar gyroviscous momentum transport rate[9-17] is of the same order as inferred from experiment and has been found to agree with measured momentum confinement times in a number of tokamaks[18] as well as in DIII-D[19,20]. Calculation of momentum transport rates from gyro-fluid microinstability models are also under development[21].

2. Work on Plasma Rotation in DIII-D

Earlier work on the first-principle calculation of plasma toroidal and poloidal rotation, including a first-principle calculation of neoclassical gyroviscous momentum transport, was collected and extended to provide a basis for analysis of DIII-D rotation data[22,23]. Predicted momentum confinement times and rotation velocities are compared with experimental values in Table 3. With the exception of the last shot, which is the only one with an internal transport barrier, the gyroviscous prediction of the momentum confinement time is in agreement with the measured value, over a wide range of confinement modes and beam powers.

Table 3: Comparison of Predicted and Measured Toroidal Rotation Speeds and Momentum Confinement Times in DIII-D

Shot Time	Mode, NBI, impurity	P_{nbi} MW	$\overline{n}$ m^{-3}	T_{i0}, T_{e0} keV	$V_{\phi 0}$ / V_{thD}	τ_φ^{th} ms	τ_φ^{exp} ms	$V_{\varphi 0}^{th}$ 10^5m/s	$V_{\varphi 0}^{exp}$ 10^5m/s
98777 1.6 s	L, Co Carbon	4.5	3.42	3.5 2.5	0.31	80	73	1.52	1.50
98775 1.6 s	L, Co Neon	"	4.05	6.3 3.3	0.37	147	152	2.90	3.06
99411 1.8 s	H, Co Carbon	9.2	4.80	8.3 3.9	0.32	93	84	2.90	2.64
106919 2.0 s	QH, Ctr Ni-Cu,	9.32	2.58	10.9 3.9	0.40	44	45	3.86	3.98
" 3.5 s	"	"	2.83	14.2 4.2	0.38	64	68	4.21	4.48
106956 3.1 s	QDB Ctr CuNi,	11.77	3.75	15.1 4.4	0.24	44	46	2.41	2.51
102942 0.85 s	H, Co Carbon	4.89	2.36	1.8 2.5	0.40	55	51	2.20	2.02
" 1.25 s	ITB, Co Carbon	7.08	2.67	4.8 4.2	0.35	52	72	2.94	4.01

The radial distributions of the calculated toroidal and poloidal rotation velocities are compared with the measured rotation velocities of the carbon impurity species for one of the shots in Figs. 2 and 3. The gyroviscosity expression is the product of a constant depending on temperature, major radius and toroidal field, a factor Θ which depends on the calculated poloidal density asymmetries and the poloidal rotation velocities, and a factor G which depends on the radial density, temperature and velocity gradient scale lengths estimated from experimental data. The toroidal rotation calculation is shown for the best estimate of the factor ΘG and for a value twice as large. The agreement between the predicted and measured velocities is improved by enhancing the gyroviscous momentum transport rate, in this shot, perhaps indicating that some other transport mechanism is also involved.

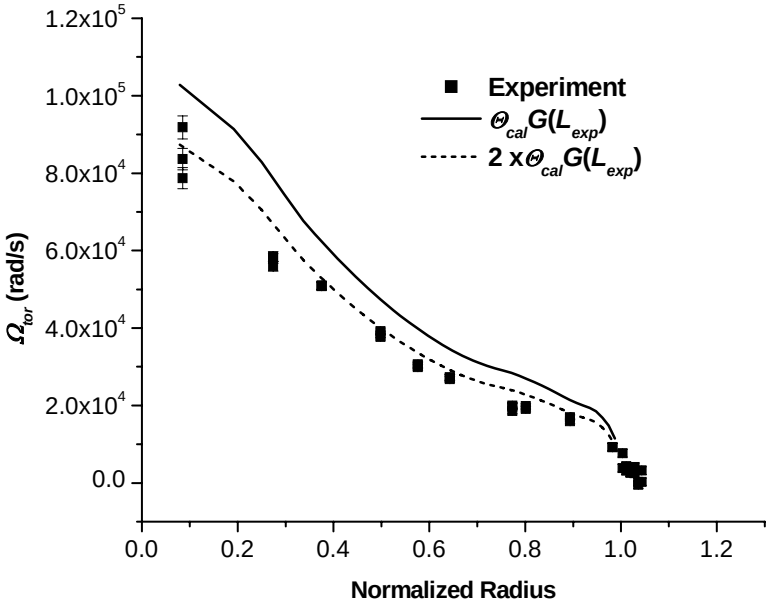

Figure 2: Comparison of the calculated toroidal angular velocity Ω_ϕ with experiment for different values of the product ΘG (DIII-D shot 98777 @ 1.6 s)

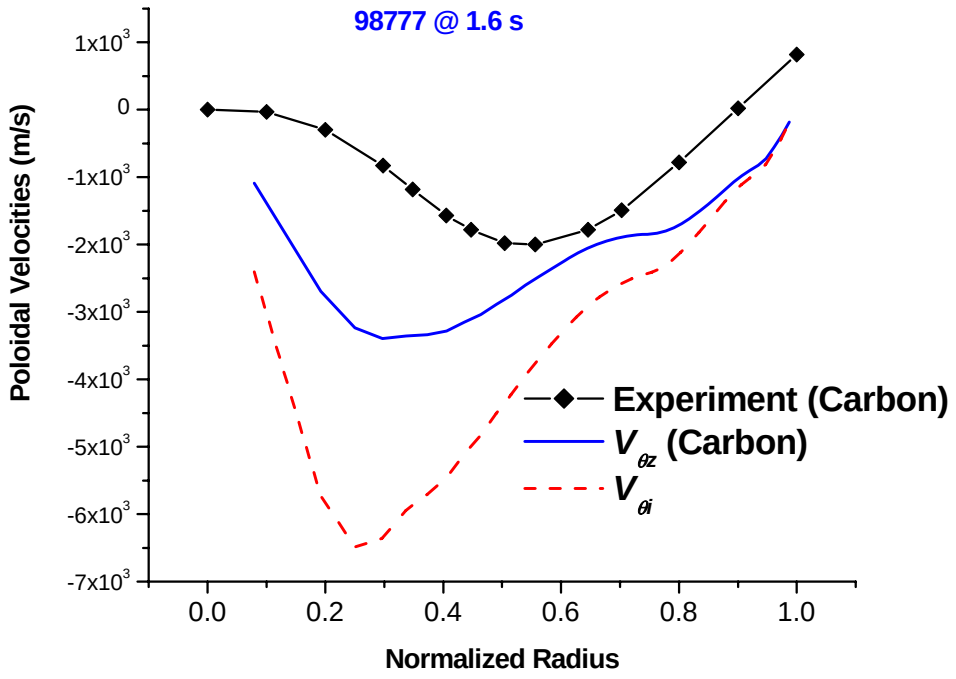

Figure 3: Comparison of the calculated poloidal velocities with experiment. (DIII-D shot 98777 @ 1.6 s)

We note that there has been some confusion on the existence and magnitude of neoclassical gyroviscosity. While the gyroviscous neoclassical theory is well documented[9-17], it is not so familiar as the perpendicular neoclassical momentum transport theory nor was it reported in three contemporary developments[6-8] of momentum transport theory based on gyroradius ordering schemes. In these gyroradius ordering developments[6-8], both the poloidal rotation and the gyroviscosity vanished to leading order. Further investigation of the gyroradius ordering development showed that a poloidal rotation velocity of the order seen experimentally and a non-vanishing gyroviscosity were obtained in the next order. Numerical calculations[18-20] demonstrated that, even though the velocity gradients in the gyroviscosity were smaller than those in the perpendicular viscosity, when the much larger coefficient of gyroviscosity was taken into account the gyroviscosity was two orders of magnitude larger than the perpendicular viscosity reported in these papers and should not be ordered out on the basis of the velocity gradients alone.

3. References on Rotation

1. A. M. Garofalo, et al., Nucl. Fusion, 41, 1171 (2001).
2. K. H. Burrell, Phys. Plasmas, 4, 1499 (1997).
3. E. Hameiri, Phys. Plasmas, 5, 3270 (1998).

4. W. M. Stacey, Phys. Plasmas, 8, 158 (2001).
5. J. S. deGrassie, et al., Nucl. Fusion, 43, 142 (2003).
6. F. L. Hinton and S. K. Wong, Phys. Fluids, 28, 3082 (1985).
7. J. W. Connor, et al., Plasma Phys. Control. Fusion, 29, 919 (1987).
8. S. K. Wong and V. S. Chan, Phys. Plasmas, 11, 3432 (2004).
9. A. N. Kaufmann, Phys. Fluids, 3, 610 (1960).
10. S. I. Braginskii, Rev. Plasma Phys., 1, 205 (1965).
11. A. B. Mikhailovskii and V. S. Tsypin, Sov. J. Plasma Phys., 10, 51 (1984).
12. W. M. Stacey and D. J. Sigmar, Phys. Fluids, 28, 2800 (1985).
13. R. H. Hazeltine and J. D. Meiss, "Plasma Confinement", Addison-Wesley, Reading MA (1994), pp 208, 220 and 226.
14. W. M. Stacey, Phys. Fluids B, 4, 3302 (1992).
15. A. L. Rogister, Phys. Plasmas, 1, 619 (1994).
16. H. A. Claassen, et al., Phys. Plasmas, 7, 3699 (2000).
17. A. N. Simakov and P. J. Catto, Phys. Plasmas, 10, 4744 (2003); also, Contrib. Plasma Phys., 44, 83 (2004).
18. W. M. Stacey and D. R. Jackson, Phys. Fluids B, 5, 1828 (1993).
19. W. M. Stacey and M. Murakami, Phys. Plasmas, 8, 4450 (2001).
20. W. M. Stacey and J. Mandrekas, Phys. Plasmas, 9, 1622 (2002).
21. G. M. Staebler, General Atomics, private communication (2004).
22. W. M. Stacey, "Neoclassical theory for rotation and impurity transport in tokamaks with neutral beam injection", Phys. Plasmas, 8, 158 (2001).
23. W. M. Stacey, "Neoclassical calculation of poloidal rotation and poloidal density asymmetries in tokamaks", Phys. Plasmas, 9, 3874 (2002).
24. W. M. Stacey and M. Murakami, "Momentum confinement in DIII-D shots with impurities", Phys. Plasmas, 8, 4450 (2001).
25. W. M. Stacey, "The role of neoclassical convection in the confinement improvement of plasmas with impurity injection in DIII-D", Phys. Plasmas, 8, 3689 (2001).
26. W. M. Stacey and J. Mandrekas, "Comparison of neoclassical rotation theory with experiment under a variety of conditions in DIII-D", Phys. Plasmas, 9, 1622 (2002).

D. NEUTRAL TRANSPORT

1. Background

The importance of neutral atoms to the performance of tokamak plasmas is widely recognized. Not only does the fueling of the core plasma by gas-injection and recycling depend on the transport of neutral particles through the plasma edge and divertor region, but a number of other important phenomena are sensitive to the neutral concentration in the plasma edge. For example, there is experimental evidence that the H-L transition, the density limit and the formation of the edge pedestal are all sensitive to the neutral concentration in the plasma edge.

Most codes presently available that can treat neutral transport in the complicated geometrical regions with strongly varying mean-free-path that characterize the edge and divertor regions of tokamaks are based on the Monte Carlo method. However, Monte Carlo calculations are very time consuming and their use, particularly in iterative, coupled plasma fluid—Monte Carlo neutrals calculations, is restricted. Moreover, the inherent numerical noise present in Monte Carlo simulations makes convergence difficult.

Thus, there is a need for a fast and accurate 2D neutrals code that can be used routinely for the analysis of tokamak experiments.

We have developed an interface current balance formulation of integral transport theory in which the transport of uncollided neutrals is treated exactly, while the effect of charge-exchange and elastic scattering across regions is treated approximately by means of escape probabilities[1]. The TEP methodology has been implemented into the 2D neutral transport code GTNEUT[2].

The TEP methodology and the GTNEUT code have been extensively tested by comparison with Monte Carlo[3] calculations for a series of model problems designed to be sensitive to the approximations made in the TEP methodology and its implementation in the current version of GTNEUT. These test comparisons[4-5] confirmed the basic TEP transport methodology over a wide range of the parameter Δ/λ, where Δ is the characteristic dimension of a computational region (equivalent to the grid size of a structured grid) and λ is the neutral mean-free-path.

2. Work on Neutral Transport in DIII-D

The TEP methodology has been an important component in several computational tools employed in the Georgia Tech – DIII-D collaboration. Simplified versions of the method have been implemented in the codes used in the first two research tasks described in this report. The full GTNEUT code has also been used to analyze DIII-D neutral density experiments[6] and to analyze and evaluate DIII-D pumping scenarios.

Analysis of DIII-D neutral density experiments

The neutral density in the vicinity of the X-point has recently been measured[7] in both L-mode and H-mode discharges in DIII-D. These discharges have been calculated with both GTNEUT and DEGAS, using the same 2-D geometry, the same background plasma properties (computed with the 2-D plasma fluid code B2.5), the same atomic reaction rate data, and the same carbon wall reflection model. Since the GTNEUT code cannot handle the transport of molecular species yet, the DEGAS code was run with and without molecular transport to facilitate the GTNEUT-DEGAS comparison.

First, we compared[6] the predictions of the GTNEUT and DEGAS codes with the experimental neutral measurements for the L-mode DIII-D discharge #96740 at 2250 ms. The geometric model is shown in Fig. 4. The X-point in this discharge was located 13.8 cm above the divertor floor. (The z-axis in Fig. (4) is arbitrary and does not correspond to the height over the divertor floor). The shaded cells in Fig. 4 correspond to the locations at which the neutral density measurements were made.

Typical plasma densities and electron temperatures in the regions just inside the separatrix (61-63 in Fig. 1) are in the range of 3.2×10^{19} – 1.4×10^{19} m^{-3} and 50-75 eV, respectively. Densities and

temperatures are considerably lower in the private flux regions. Molecules (transported in the DEGAS, but not the GTNEUT, simulations) emerge at a wall temperature of 0.025 eV (300 °K) while atomic neutrals (used in GTNEUT and in the DEGAS simulations without molecular transport) are assumed to have Franck-Condon energies of 1 eV. The same assumptions apply to the neutrals of the gas puffing source.

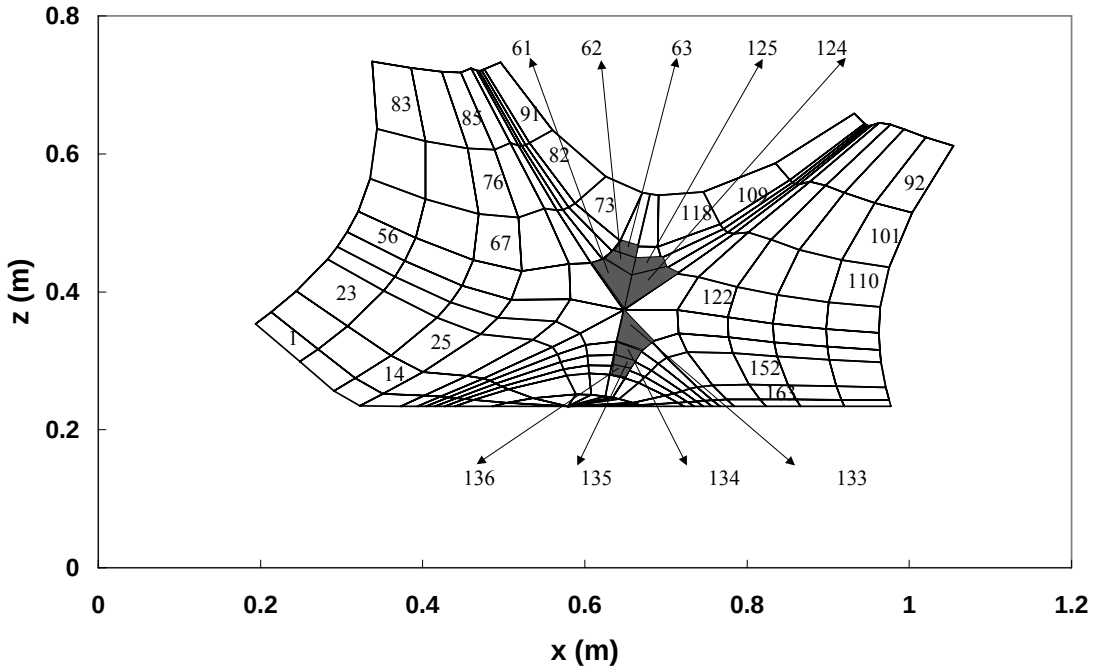

Figure 4 : Geometry used in the GTNEUT and DEGAS neutral transport simulations of DIII-D L-mode shot 96740 @ 2250 ms. Shaded regions correspond to locations where

The results of our GTNEUT and DEGAS simulations, as well as the experimental measurements and their error bars are shown in Fig. 5, where the various neutral densities are plotted vs. the height off the divertor floor. The region to the left of the separatrix line corresponds to the private flux area, and the region to the right is the core plasma.

It can be seen from Fig. 5, that the agreement between GTNEUT and the DEGAS case without molecular transport (solid circles) is excellent throughout the entire domain. The predictions of both codes (without molecular transport) agree with the experiment, being within the error bars of the measurements in all but one case. The DEGAS simulation including molecular transport under-predicts

the data in the private flux region, but is within somewhat better agreement with the measurements deep inside the plasma. These neutral measurements have also been calculated in agreement with experiment with a simplified TEP model[8] incorporated in the plasma analysis code described above.

Similar results have been obtained for the H-mode DIII-D discharge 96747 and are described in detail in Ref. 6.

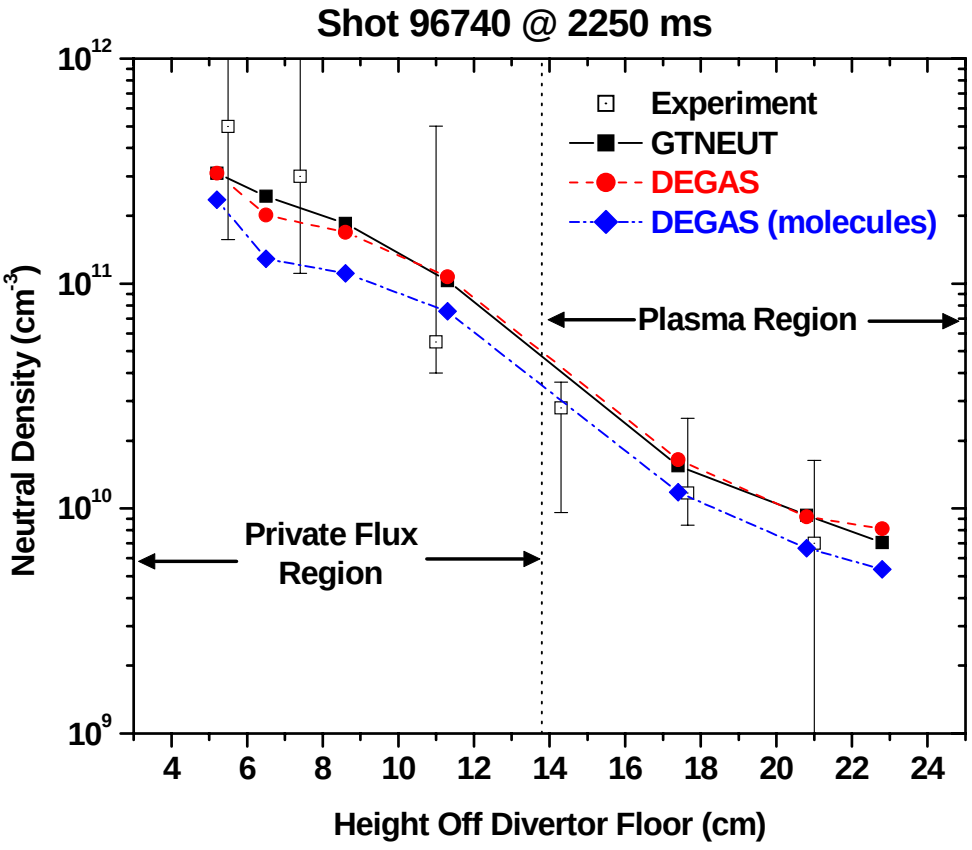

Figure 5: Comparison of GTNEUT and DEGAS simulations with experiment for the L-mode DIII-D shot 96749 @ 2250 ms.

Analysis of DIII-D pumping scenarios

GTNEUT was recently upgraded with new capabilities which greatly facilitated setting up and performing DIII-D related neutral transport simulations. These upgrades included: a) the implementation of a high performance sparse matrix solver for the solution of the resulting linear system of equations, which allows us to run much larger and therefore more realistic problems and b) the development of an

interface routine that can prepare the geometric part of the GTNEUT input file (which is the most laborious part) automatically by directly reading EFIT EQDSK files.

To test the capabilities of the upgraded code, we used it to calculate the exhaust rates from the dome and baffle pumps for the DIII-D shot 113026 @ 3000 ms (an upper single null discharge with dRsep ≈ 1.2, part of the AT Divertor Pumping series of experiments). The upper part of our geometry is shown in Fig.6 below. For the background plasma parameters (electron and ion densities and temperatures) inside the separatrix, we assumed poloidal symmetry and used the values obtained from GAProfiles. For the plasma parameters in the SOL above and below the X-point, we used experimental data provided by T. W. Petrie. For the regions where experimental data were unavailable (private flux region and the near-vacuum regions between the first wall and the last open flux surface) we used our judgment to assign arbitrary but reasonable background plasma parameters.

The results of our simulation predicted an exhaust rate ratio $\Gamma_{dome} / \Gamma_{baffle} = 0.88$. This result agrees very well with the measured ratio for dRsep = 1.2, as can be seen from Fig. 7.

The results of our neutral transport simulations depend on the ion and neutral recycling assumptions. Since no detailed information on the location and magnitude of the recycling sources was available for this shot, our reference simulation assumed in/out symmetry and equal recycling sources from the divertor segments adjacent to the dome and baffle pump entrances (wall segments 84, 86, 93, 95 in Fig. 6). This is a reasonable assumption given the flux expansion between the X-point and the strike points and the experimental indication of comparable recycling rates from inside and outside. The magnitude of the recycling sources was arbitrary (a crude estimate from the in/out ion flows at the pre-sheath) but this is not very important since we were interested in the ratio of the exhaust rates.

To test the sensitivity of our simulations to these uncertainties, the $\Gamma_{dome} / \Gamma_{baffle}$ ratio was calculated for different recycling assumptions ranging from uniform recycling (MCR or main chamber recycling) to various combinations of recycling flux ratios. These results are shown in Table 4. It can be seen that the $\Gamma_{dome} / \Gamma_{baffle}$ ratio is a sensitive function of the location of the recycling source.

It should be emphasized that our calculation was meant to demonstrate and test the new capabilities of our code and is not a definite calculation of the DIII-D pumping rates. We plan a more detailed series of simulations working in close contact with DIII-D scientists to ensure that we use the best information available on background plasma parameters and recycling sources.

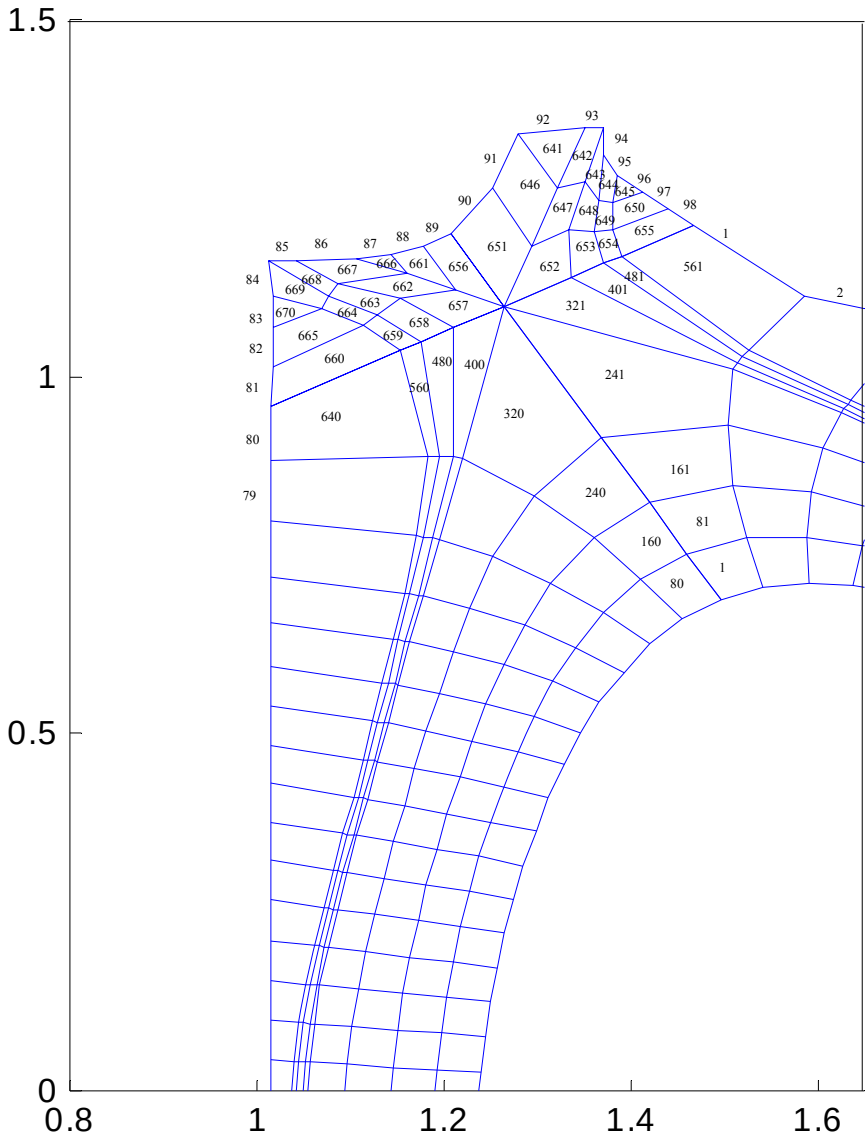

Figure 6: Upper part of DIII-D geometry used by GTNEUT for the analysis of DIII-D shot 113026 @ 3000 ms. The dome and baffle pump openings are represented by wall segments 85 and 94 respectively.

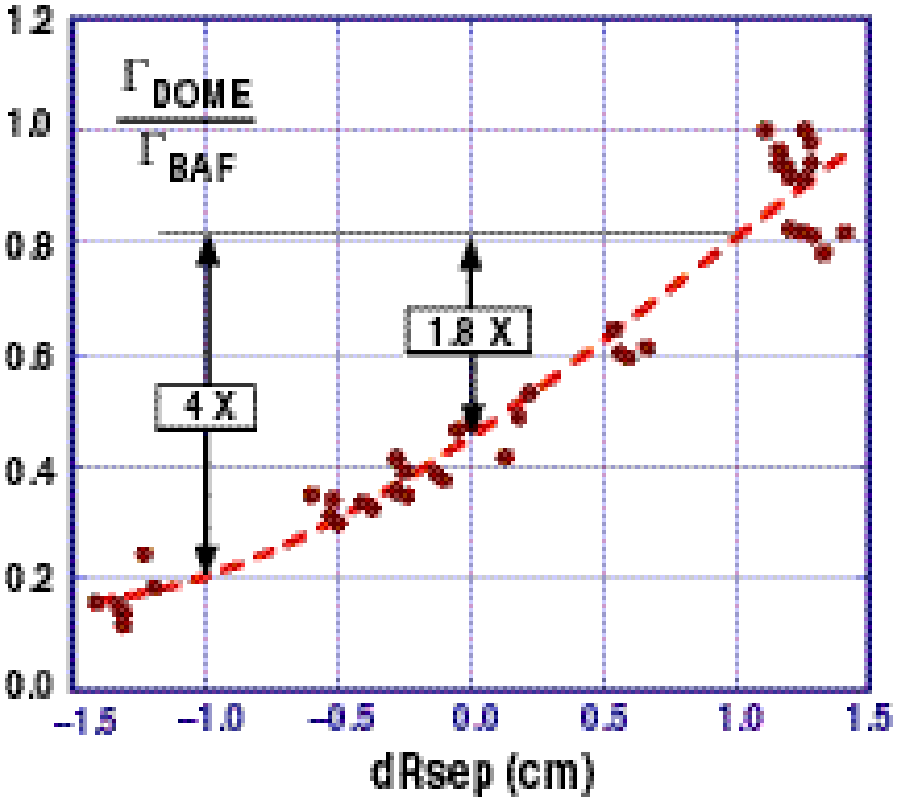

Figure 7: Experimental Γ_{dome} / Γ_{baffle} ratio vs. dRsep (T.W. Petrie, et al.)

Flux distribution	Γ_{dome} (#/s)	Γ_{baffle} (#/s)	Γ_{dome} / Γ_{baffle}
$\Phi_{84}=\Phi_{86}=\Phi_{93}=\Phi_{95}$	0.5695×10^{22}	0.6426×10^{22}	0.88
Uniform (MCR)	0.613×10^{21}	0.71×10^{21}	0.86
$\Phi_{86}=\Phi_{93}$, $\Phi_{84}=\Phi_{95}=0$	0.192×10^{22}	0.924×10^{22}	0.20
$\Phi_{86}=1.5\times\Phi_{84}$ $\Phi_{93}=\Phi_{95}$	0.494×10^{22}	0.643×10^{22}	0.76
$(\Phi_{84}+\Phi_{86})/(\Phi_{93}+\Phi_{95})=0.5$	0.380×10^{22}	0.855×10^{22}	0.45
$(\Phi_{84}+\Phi_{86})/(\Phi_{93}+\Phi_{95})=2.0$	0.760×10^{22}	0.430×10^{22}	1.77

Table 4: Sensitivity of the ratio to various recycling assumptions. The total recycling source is kept constant for all cases and equal to 1.0×10^{23} #/s. Numerical subscripts correspond to the GTNEUT wall numbering scheme (see Fig. 6).

Two of the basic assumptions of the TEP methodology are the assumption of an isotropic neutral distribution function in both the inward and outward half-spaces at the interfaces between the computational regions, and the assumption of a uniform charge exchange collision source within the volume of each cell. The first assumption, also known as the DP_0 approximation, has been shown to be a good approximation since charge exchange and elastic scattering collisions tend to isotropize the neutral

distribution function. However, departures from anisotropy are possible, especially in long mean free path regions where anisotropies driven by wall reflection, presence of vacuum regions, pumps, etc. would persist across regions. Extending the original DP_0 approximation to include linearly (DP_1) and quadratically (DP_2) anisotropic distributions appears to resolve this issue, as evidenced by comparisons with Monte Carlo for model problems designed to accentuate the anisotropy effects[9].

The second assumption, i.e. the uniformity of the charge exchange collision source is embodied in the rational approximation that we employ for the first flight collision probability. This assumption may become questionable in regions where the neutral mean free path λ is much smaller than the characteristic dimension of the cell Δ. In these regions, the first collision source is predominantly located near the incident interface, resulting in a preferential backscattering of these neutrals across that incident surface. Work to address this problem is in progress as part of the Ph.D thesis of D-K. Zhang.

Finally, a long-term goal of our GTNEUT development is the coupling of our code with the 2D edge fluid code UEDGE[10]. Preliminary results show that the implementation of GTNEUT into UEDGE will improve UEDGE's treatment of neutral transport[11].

3. References for Neutral Transport

1. W. M. Stacey and J. Mandrekas, "A Transmission-Escape Probabilities Model for Neutral Particle Transport in the Outer Regions of a Diverted Plasma", Nucl. Fusion, 34, 1385 (1994).
2. J. Mandrekas, "GTNEUT: A code for the calculation of neutral particle transport in plasmas based on the Transmission and Escape Probability method," Comput. Phys. Comm. 161, 36 (2204).
3. Heifetz, D., Post., D., Petravic, D., et al., J. Comput. Phys. 46, 309 (1982).
4. W. M. Stacey, J. Mandrekas and R. Rubilar, "Interface Current Integral Transport Methods for the Calculation of Neutral Atom Transport in the Edge Region of Fusion Plasmas", Fusion Sci. Technol., 40, 66 (2001).
5. R. Rubilar, W. M. Stacey and J. Mandrekas, "Comparison of the TEP Method for Neutral Particle Transport in the Plasma Edge with the Monte Carlo Method", Nucl. Fusion, 41, 1003 (2001).
6. J. Mandrekas, R. J. Colchin, W. M. Stacey, et al., "Analysis of Recent DIII-D Neutral Density Experiments", Nucl. Fusion 43 (2003) 314.
7. Colchin, R.J., et al., Nucl. Fusion 40, 175 (2000).
8. W. M. Stacey, "Modeling the neutral density in the edge of the DIII-D plasma", Nucl. Fusion, 40,965 (2000).
9. Dingkang Zhang, J. Mandrekas and W.M. Stacey, "Extensions of the TEP Neutral Transport Methodology", Contrib. Plasma Phys. 44, 45 (2004).
10. F. Wising et al., Contrib. Plasma Phys. 36, 136 (1996).
11. J. Mandrekas, M.V. Umansky, D. Zhang, "Comparative study of neutral transport models for edge plasmas,' to be presented at the 46th APS DPP meeting, 2004.

E. IMPURITY TRANSPORT

1. Background

During our participation in the ITER EDA, we developed advanced computational tools for the analysis of impurity transport in tokamak plasmas. This involved the implementation of a multi species and multi charge state impurity transport module into our time-dependent 1½-D core transport code GTWHIST[1-3]. While the original motivation for this work was to perform coupled, self-consistent main plasma – impurity transport simulations in order to determine the feasibility of an impurity-seeded radiating mantle as a mechanism for the reduction of the exhaust power from the plasma core, the computational capability that was developed is useful in any situation involving external or intrinsic impurities in a plasma.

2. Previous Work on Impurity Transport under Grant ER54538

Analysis of RI-mode DIII-D Discharges

During the Georgia Tech – DIII-D Collaboration, we used these computational tools to analyze several DIII-D discharges with non-intrinsic seeded impurities (Ne, Ar and Kr)[4]. Although the original motivation for the injection of external impurities into DIII-D had been edge profile modification for AT operation, recent observations (in DIII-D and other tokamaks worldwide) of significant confinement improvement following impurity injection due to suppression of core turbulence have made impurity seeding an important tool for the understanding of transport mechanisms in tokamak plasmas and for the comparison of theory-based turbulence and transport models with experiment.

Most of our recent effort was in the analysis of a series of L-mode, negative shear, DN discharges exhibiting various degrees of confinement improvement in most transport channels following impurity injection (shots 98775-98794 and 103205-103209). This confinement improvement has been attributed to the synergistic effect of impurity induced enhancement of the $E \times B$ shearing rate and reduction of the drift wave turbulence growth rate[5].

Our coupled main plasma – impurity transport simulations were predictive in nature (in the sense that our transport code was run in predictive mode, not making any use of measured plasma or impurity profiles) but with a small number of adjustable coefficients (mainly amplitudes of the plasma and impurity charge state transport coefficients, strength and location of impurity source, etc.). We found that using simple empirical and semi-empirical transport models for the transport of the impurity charge states and the main plasma particle and energy transport, we were able to obtain very good agreement between simulation and experiment. A typical comparison between simulation and experiment is shown in Fig. 8, where various profiles from our simulation are compared with the experimental measurements for the Neon injected shot 98775.

Our simulations indicated that, while energy transport was reduced to almost neoclassical levels in these impurity seeded discharges, impurity transport was not neoclassical. In addition, we concluded

that the observed reduction of the Carbon concentration in the core was due to the reduction of the wall carbon source rather than due to transport effects.

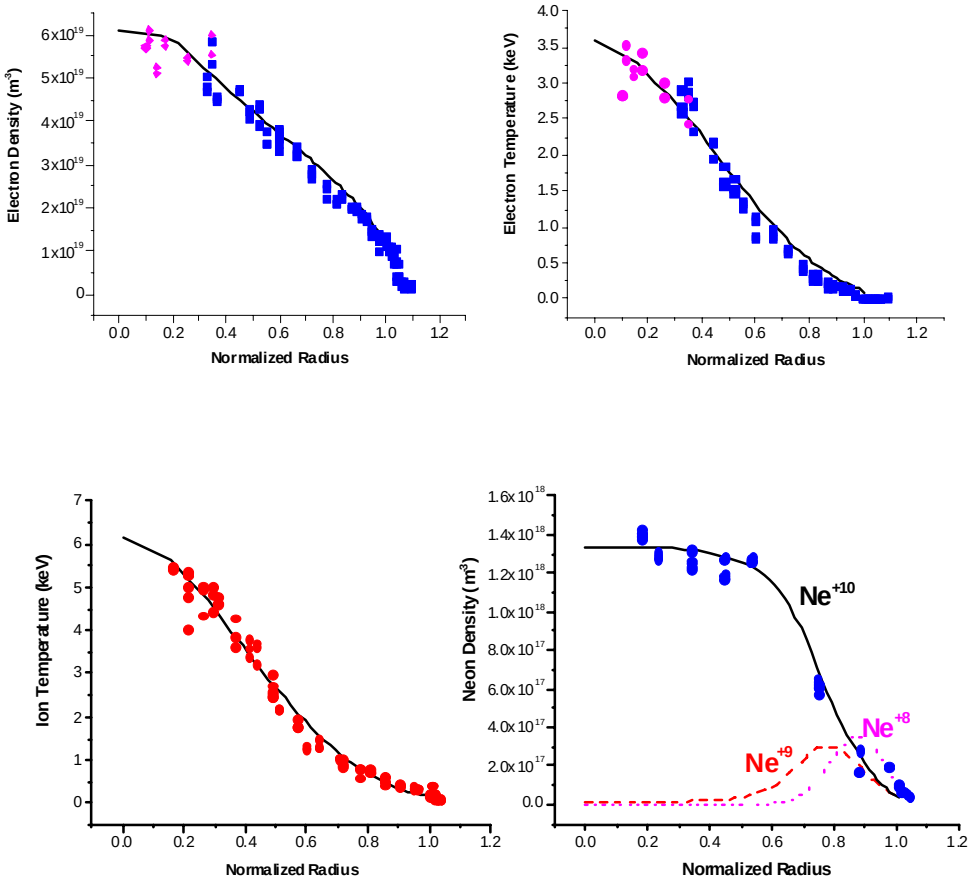

Figure 8: Comparison of simulation and experiment for various main plasma and impurity profiles for shot 98775 at 1.6 s.

The results of our simulations were useful not only because they helped us understand impurity transport in DIII-D, but also because they provided us with self-consistent Z_{eff} profiles (including the contribution from all charge states and not only from the ones that were measured) as well as with profiles of the various impurity charge states. This profile information was then used as input to gyrokinetic or gyrofluid codes to make quantitative tests of theory-based turbulence models with experimental measurements[5-6].

Neoclassical Impurity Transport Analysis of QDB Discharges

A series of multi-species impurity transport simulations using the neoclassical impurity transport code NCLASS[7] were performed in order to determine whether the observed strong high-Z impurity accumulation in recent Quiescent Double Barrier (QDB) DIII-D discharges (shots 106919 and 106972) is consistent with the predictions of neoclassical theory.

The simulations were performed for a fixed background plasma, using fits to the various measured profiles (n_e, T_e, T_i, various impurity charge states for C^{+6}, $Ni^{24\text{-}28}$, etc.). The various MHD metric coefficients required by NCLASS have been computed using the appropriate EFIT EQDSK files ("g" files) for this shot.

The total neoclassical particle flux and its various components for the Ni^{+26} state at t = 3510 ms for shot #106919 are shown in Fig. 9. Shown in Fig. 9 are the total flux, the banana-plateau (BP) flux, the Pfirsch-Schlüter (PS) flux, the classical (CL) flux and the flux due to the $\langle \mathbf{E} \cdot \mathbf{B} \rangle$ term. It can be seen that the dominant term is the BP term, as expected since Ni^{+26} is in the banana-plateau regime.

Comparison of the calculated particle fluxes and the associated transport coefficients with the experiment revealed that the measured pinch velocities and diffusivities were much higher than the neoclassical calculations except for the very center of the plasma at $\rho < 0.1$. This would suggest that high-Z impurity transport is not described by neoclassical processes in these QDB discharges.

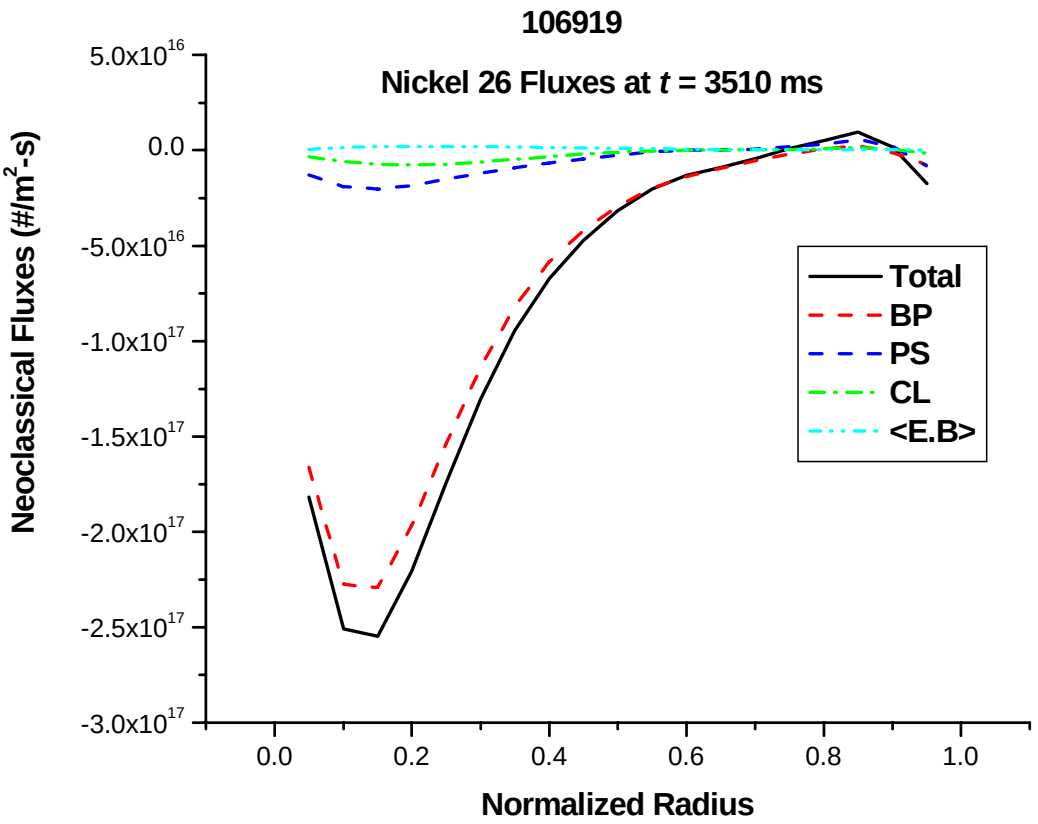

Figure 9: Total neoclassical flux and components for the Ni^{+26} charge state at 3510 ms.

3. References for Impurity Transport

1. J. Mandrekas, W.M. Stacey, *Nucl. Fusion* **35** (1995) 843.
2. J. Mandrekas, W.M. Stacey, F.A. Kelly, *Nucl. Fusion* **36** (1996) 917.
3. J. Mandrekas, W.M. Stacey, F.A. Kelly, *Nucl. Fusion* **37** (1997) 1015.
4. J. Mandrekas, W.M. Stacey, M. Murakami, M.R. Wade, G.L. Jackson, *Contrib. Plasma Phys*., **40** (2000) 498.
5. M. Murakami, et al., *Nucl. Fusion* **41** (2001) 317.
6. M. Murakami, et al. *Physics of Confinement Improvement of Plasmas with Impurity Injection in DIII-D*, 18th IAEA Fusion Energy Conference, Sorrento, Italy, 2000.
7. W.A. Houlberg, K.C. Shaing, S.P. Hirshman, and M.C. Zarnstorff, Phys. Plasmas **4** (1977) 3230.
8. W. P. West, M.R. Wade, C.M. Greenfield, et al. *Phys. Plasmas*, **9** (2002) 1970.